9-25-2015

High Temperature Oxidation Kinetics of Dysprosium Particles

Brian J. Jaques
Boise State University

Darryl P. Butt
Center for Advanced Energy Studies

Publication Information

Jaques, Brian J. and Butt, Darryl P.. (2014). "High Temperature Oxidation Kinetics of Dysprosium Particles". *Journal of Alloys and Compounds, 644,* 211-222. https://doi.org/10.1016/j.jallcom.2015.04.174

Journal of Alloys and Compounds 644 (2015) 211–222

Contents lists available at ScienceDirect

Journal of Alloys and Compounds

journal homepage: www.elsevier.com/locate/jalcom

High temperature oxidation kinetics of dysprosium particles

Brian J. Jaques, Darryl P. Butt *

Department of Materials Science and Engineering, Boise State University, 1910 University Dr., Boise, ID 83725, USA
Center for Advanced Energy Studies, 995 University Blvd., Idaho Falls, ID 83415, USA

ARTICLE INFO

Article history:
Received 28 January 2015
Received in revised form 14 April 2015
Accepted 25 April 2015
Available online 1 May 2015

Keywords:
Dysprosium
Oxidation
Kinetics
Gas–solid reactions
Rare earth alloys and compounds
Corrosion

ABSTRACT

Rare earth elements have been recognized as critical materials for the advancement of many strategic and green technologies. Recently, the United States Department of Energy has invested many millions of dollars to enhance, protect, and forecast their production and management. The work presented here attempts to clarify the limited and contradictory literature on the oxidation behavior of the rare earth metal, dysprosium. Dysprosium particles were isothermally oxidized from 500 to 1000 °C in N_2–(2%, 20%, and 50%) O_2 and Ar–20% O_2 using simultaneous thermal analysis techniques. Two distinct oxidation regions were identified at each isothermal temperature in each oxidizing atmosphere. Initially, the oxidation kinetics are very fast until the reaction enters a slower, intermediate region of oxidation. The two regions are defined and the kinetics of each are assessed to show an apparent activation energy of 8–25 kJ/mol in the initial region and 80–95 kJ/mol in the intermediate oxidation reaction region. The effects of varying the oxygen partial pressure on the reaction rate constant are used to show that dysprosium oxide (Dy_2O_3) generally acts as a p-type semiconductor in both regions of oxidation (with an exception above 750 °C in the intermediate region).

1. Introduction

Global interest in rare earth element production and management has significantly increased in the past few years. In the year 2008, nearly $190 million worth of rare earth materials were imported and used in the U.S. alone. Such "strategic materials" are sought after for use in metallurgical applications and alloys, electronics, catalysts, and cathode ray tubes [1]. Compared to the light rare earth metals, relatively little published literature exists for praseodymium, promethium, thulium, lutetium, and dysprosium (also known as the heavy rare earths) although scientific interest in these metals is on the rise. In the next forty years, Hoenderdaal et al. [2] project that the demand for dysprosia (Dy_2O_3) and other dysprosium compounds will increase to between 7 and 25 times (to 14–50 ktons) from the 2010 demand. Modern studies suggest that dysprosium is more abundant than 44 other elements in the earth's crust (5.2 mg/kg) contrary to earlier perception, making its utility more available for emerging materials technologies [3].

According to Hoenderdaal et al. [2], the proposed increase in demand is due to the future of magnetic applications (electric motors) due to dysprosium's exceptional magnetic moment of 10.8 Bohr magnetrons, which is second only to holmium [3], and its ability to induce coercivity as an alloying agent or dopant [3,4]. However, the demand for dysprosium has become more prevalent in other applications due to its many other interesting properties. For instance, dysprosium's isotopes strongly absorb neutrons which lead to its use in nuclear reactor control rod moderator materials [3,5–7] and Dy_2O_3 has been considered as a substitute for SiO_2 in high-k dielectric applications due to its large band gap (4.9 eV) and dielectric constant (14) [8,9]. Additionally, dysprosium mononitride (DyN) has been postulated as a suitable surrogate for americium mononitride (AmN) due to its similar physical and chemical attributes in studying its sintering and alloying effects in spent nuclear fuel reprocessing [10–15]. DyN has also been investigated as a material for ferromagnetic and semiconductor superlattice structures for spintronic applications [16–18].

Although a few manuscripts and reports were published in the late 1950s and 1960s on the oxidation behavior of dysprosium [19–22], the experiments were performed on monolithic samples (rather than powders or particles) and the results appeared to be contradictory. Of particular interest in this study is the high temperature oxidation kinetics of elemental dysprosium in the temperature range of 450–1000 °C in N_2–(2%, 20%, and 50%) O_2 and Ar–20% O_2 using simultaneous thermal analysis techniques. An understanding of the oxidation kinetics of dysprosium has a wide

* Corresponding author at: Boise State University, 1910 University Drive, Boise, ID 83725-2075, USA. Tel.: +1 208 426 1054.
E-mail address: DarrylButt@BoiseState.edu (D.P. Butt).

http://dx.doi.org/10.1016/j.jallcom.2015.04.174
0925-8388/Published by Elsevier B.V.

range of implications ranging from semiconductor and electronics applications, to "green" energy and electric motor (magnetic) applications, to nuclear power generation applications.

2. Experimental details

The starting material used to study the high temperature oxidation kinetics of dysprosium was dysprosium particles (99.7 wt% purity, ESPI) sieved through a 40 mesh (420 μm) sieve (Fig. 1). The particles had a surface area of $0.20 \pm 0.06\ m^2\ g^{-1}$, as determined by nitrogen adsorption Brunauer–Emmett–Teller (BET) techniques. The particles were characterized using X-ray diffraction (XRD) with a Cu Kα source, as shown in Fig. 2. Additionally, minor concentrations of iron, yttrium, terbium, and tungsten (<3 ppm each) were identified in the starting material using a Thermo XSeries II quadrupole inductively coupled plasma mass spectrometry (ICPMS).

Oxidation experiments were performed using a high resolution simultaneous thermal analyzer (Netzsch STA 449) which is capable of collecting thermogravimetric analysis (TGA) and differential scanning calorimetry (DSC) data simultaneously. Approximately 30 mg of the dysprosium particles (sealed and stored in an argon filled glovebox) was loaded into an 85 μL alumina combustion crucible which was immediately loaded in the STA furnace. In each case, a vacuum purge cycle was started using an oxygen-gettered ultra high purity (UHP) argon gas (<1 ppb oxygen). Once the chamber was fully purged, the thermal profile was started. The four process gases used for the oxidation studies presented in this manuscript were certified mixtures of N_2–(2%, 20%, and 50%) O_2 and Ar–20% O_2.

Non-isothermal oxidation data were first collected to determine suitable parameters to study the isothermal oxidation behavior. In the non-isothermal experiments, the furnace was ramped from 25 to 1100 °C at 20 °C/min in a gas flow rate of 100 mL/min while TGA and DSC data were collected. Each data set was replicated at least twice and the results were averaged. Isothermal oxidation experiments were completed in each of the atmospheres from 500 to 1000 °C. In each case, the temperature of the furnace was allowed to equilibrate for 5 min at the desired temperature prior to introducing the oxidizing atmosphere and the dysprosium particles were oxidized to completion. Each isothermal oxidation experiment was repeated 3–4 times. The isothermal oxidation data were averaged together and then the average mass gain was normalized by subtracting the initial mass gain (which was less than 0.1% in all cases). To account for geometry, the data was then divided by the maximum mass obtained and then multiplied through by the specific surface area (where the specific surface area is equal to the initial mass multiplied by the surface area of the particles obtained from B.E.T., as described above). This allowed for a direct comparison of data and accurate kinetics analysis using the specific mass gain with units of $\mu g/cm^2$.

3. Results and discussion

Dysprosium is reported to have a hexagonal close packed (HCP) crystal structure and a melting temperature of 1412 °C [3], although there also exists two other allotropes; a low temperature (<−187 °C) orthorhombic phase (Cmcm) and a high temperature (>1381 °C) face centered cubic (FCC) phase ($Im\bar{3}m$) [3]. As seen in Fig. 2, the starting material for the oxidation studies presented here is primarily a HCP dysprosium phase (P63/mmc) with a small fraction of the high temperature FCC phase. The HCP and FCC cubic phases were identified using X-ray diffraction data from the International Centre for Diffraction Data (ICDD) database provided by Spedding et al. [23] and Curzon et al. [24], respectively. Additionally, it is important to note that the diffraction peaks were slightly shifted from the reported positions (depicted by the diamonds and circles in Fig. 2), which is discussed in more detail later in this manuscript. Although the authors understand that the geometry and morphology of the particles are not ideal for an oxidation kinetics study, the authors were unable to identify a vendor to provide single phase dysprosium particles (with minimal oxide). However, the dysprosium particles from ESPI were nearly single phase and had a low surface area which reduced un-wanted oxidation during handling.

Fig. 2 also shows a typical diffraction pattern obtained from a fully oxidized dysprosium sample in each of the atmospheres and temperatures investigated. The particular diffraction pattern shown is the result of oxidizing the dysprosium particles completely in N_2–20% O_2 at 800 °C, which formed a cubic Dy_2O_3 phase ($Ia\bar{3}$), as compared to data in the ICDD database provided by Swanson et al. [25]. Additionally, as shown by the inverted triangles, the oxide diffraction peaks agree well with the published values for Dy_2O_3. It is also worth pointing out that there are peaks in all of the oxide diffraction patterns that were not able to be indexed, as shown in Fig. 2.

TGA and DSC data were simultaneously collected during non-isothermal oxidation of dysprosium particles in each of the

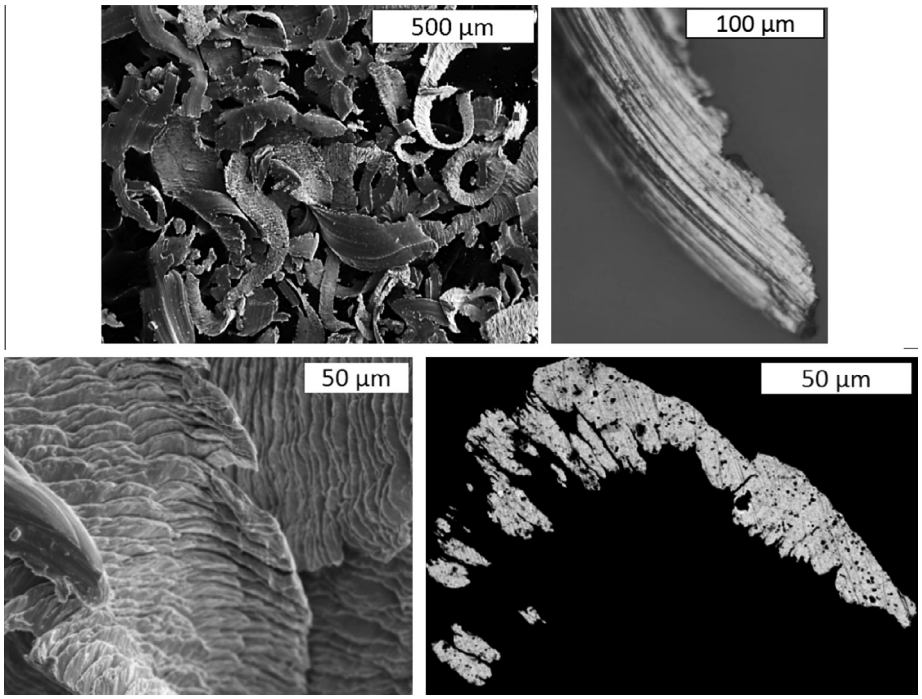

Fig. 1. Images of the dysprosium particles used as the starting materials for the high temperature oxidation reaction study. The particles have a surface area of $0.20 \pm 0.06\ m^2\ g^{-1}$ as determined via gas adsorption techniques.

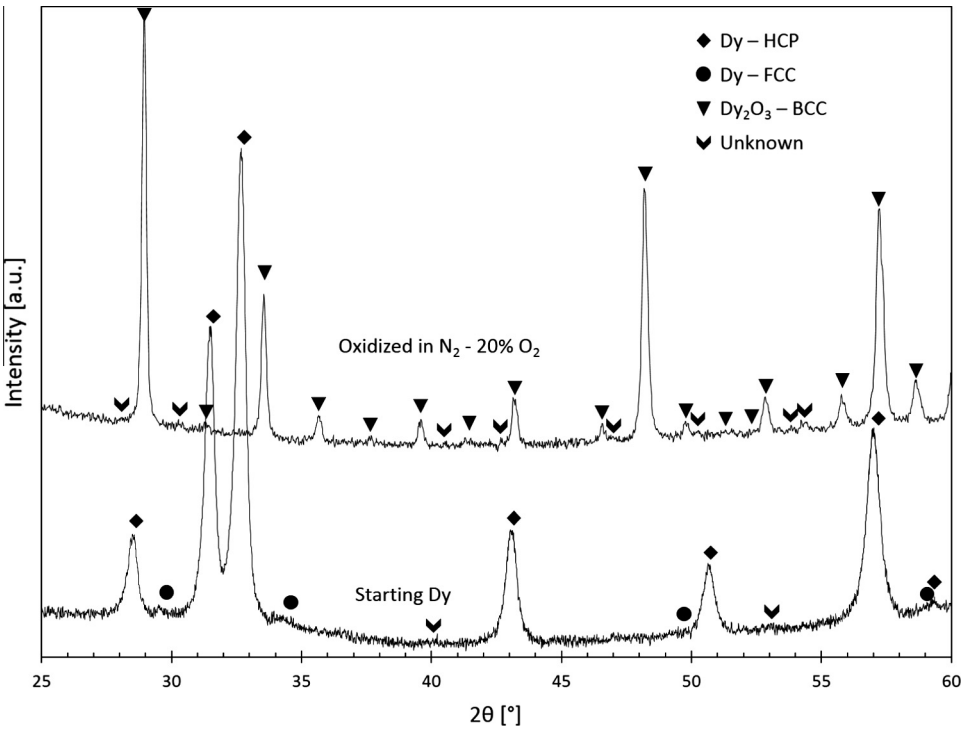

Fig. 2. X-ray diffraction patterns of the dysprosium particles used as the starting material for the high temperature oxidation study and of a sample that was isothermally oxidized in N_2–20% O_2. As seen in the figure, the starting material is primarily a HCP dysprosium phase although there does exist a very small fraction of the FCC phase. The oxidized sample is a cubic Dy_2O_3 phase and is representative of all of the oxidized powder diffraction patterns (including all environments investigated here).

atmospheres. The results are plotted in Fig. 3. From this figure, it is seen that the oxidation behavior in N_2–20% O_2 and Ar–20% O_2 is very similar throughout the entire reaction although the onset of the reaction in the nitrogen carrier gas occurs at a slightly greater temperature (approximately 20 °C). Also apparent in Fig. 3 is that the TGA trace in the N_2–50% O_2 atmosphere begins very similar to the (Ar, N_2)–20% O_2 but the kinetics slow and the TGA trace begins to deviate at approximately 50% of the total mass gain and 680 °C, as indicated by the star in Fig. 3. The deviation increases with temperature and ultimately delays the complete oxidation of dysprosium in 50% O_2 to a temperature of 960 °C, which is approximately 100 °C greater than in 20% O_2. Additionally, the TGA trace from oxidation in N_2–2% O_2 follows similar behavior as the 20% O_2 atmospheres but the onset of the reaction occurs at a slightly higher temperature: the onset of oxidation in 2% O_2 occurs at 45 °C and 26 °C greater temperatures when compared to the argon and nitrogen carriers of 20% O_2, respectively. When comparing the DSC traces in each of the oxidizing atmospheres, there exists an exothermic peak at approximately 550 °C in all atmospheres except for the oxidation reaction in N_2–2% O_2.

The results of the non-isothermal experiments informed and subsequently lead to the region of study for the isothermal oxidation temperatures reported in the remainder of this manuscript. As previously stated, isothermal oxidation experiments of dysprosium particles were completed 3–4 times at each temperature and atmosphere to arrive at average behaviors, which was used for the kinetics analysis. Fig. 4 shows typical TGA data variability between duplicated oxidation experiments. In this figure, TGA data obtained from oxidizing dysprosium particles from 650 to 800 °C in N_2–20% O_2 are used to show the typical data variability, which is minimal. The variability that is present is due to the cumulative effects of several factors, including: irregular and non-uniform particle morphology (Fig. 1), the presence of a slight amount of secondary phase in the starting material (Fig. 2), the presumed presence of a native oxide and unquantified amounts of dissolved oxygen, the likelihood of residual stresses in the starting material due to vendor processing (as indicated by the slight leftward shift in the diffraction peaks when compared to the published values [23] shown in Fig. 2), as well as the sampling technique used (i.e. a scoop sampling technique was used whereas a more effective and representative sampling technique could have been used, such as powder riffling). However, since multiple data sets were averaged for all of the analysis, the assumption is that the results are representative. It should also be noted that although the effects of particle size distribution will influence the kinetics of thermal oxidation, no effort was made in this investigation to de-convolute such effects other than to account for the starting surface area and a nominal shrinking core.

Fig. 5 shows the isothermal oxidation behavior of dysprosium particles in N_2–20% O_2 from 500 to 950 °C. Two interesting observations from Fig. 5 are: there is a distinct inflection where the oxidation kinetics slow and the specific mass gain where the inflection occurs increases with isothermal oxidation temperature. The inflection, or transition from relatively rapid to slower oxidation kinetics, is seen more clearly in Fig. 5b, which focuses on the first two minutes of the oxidation reaction. Similarly, an inflection in the mass gain rate is observed in the TGA data of all of the oxidizing atmospheres investigated, as seen in Fig. 6 for each of the four oxidizing atmospheres at 700 and 800 °C. Note that all of the TGA traces reach the same terminal specific mass gain of $5.1 \cdot 10^{-10}$ - $\mu g/cm^2$, which is based on the measured surface area and is nearly 4% less than the theoretical mass gain of the oxidation reaction. The cause of the difference is likely due to varying amounts of oxygen dissolution in the dysprosium prior to thermal treatments (predicted by Okabe et al. [26]) and variability in particle size distribution, as discussed later. Additionally, each of the TGA traces in the initial region of oxidation exhibits nearly identical mass gain

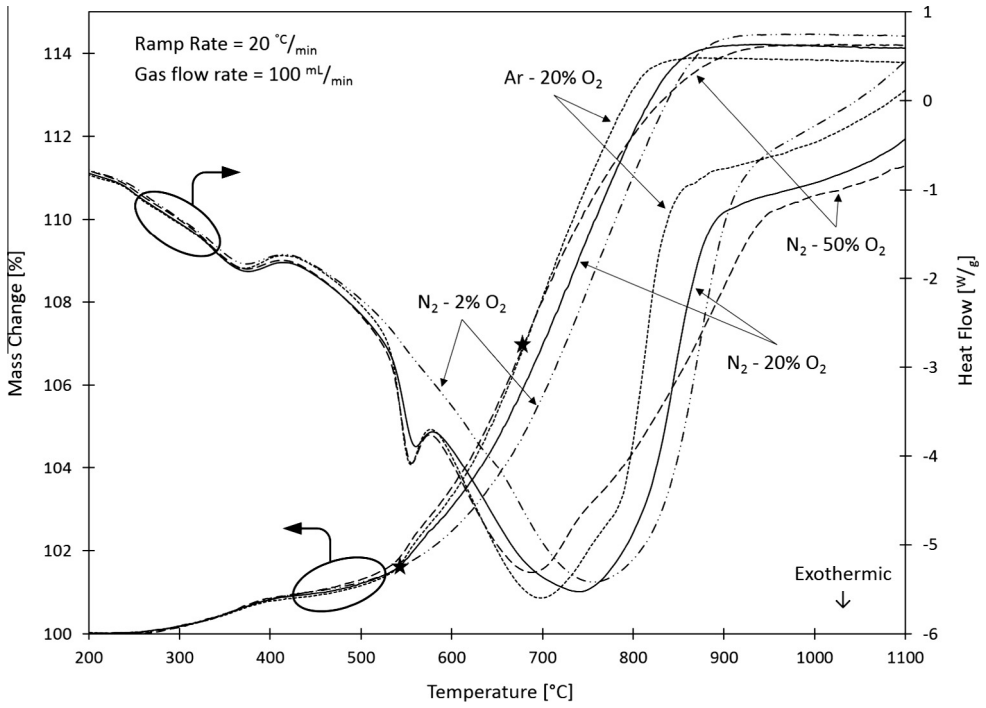

Fig. 3. Non-isothermal oxidation traces of the oxidation of dysprosium particles. The simultaneous TGA and DSC behavior is shown for each of the oxidation atmospheres investigated (N_2–(2%, 20%, or 50%) O_2 and Ar–20% O_2). The stars indicate apparent locations where deviations in mass change occur due to different oxidizing atmospheres.

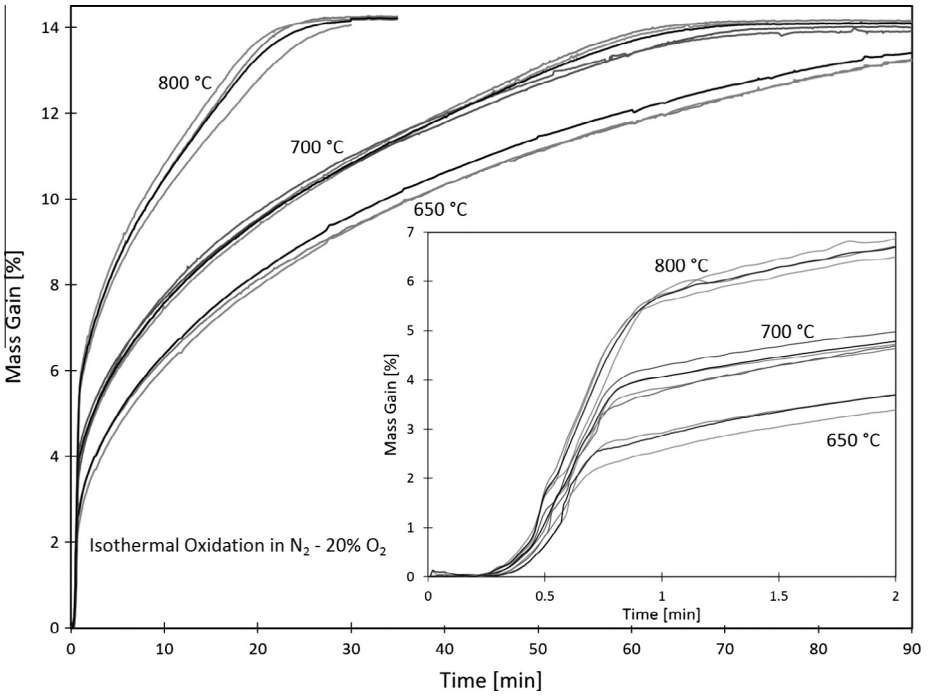

Fig. 4. Typical isothermal TGA traces used for the kinetics assessment of the oxidation of dysprosium particles in N_2–20% O_2. The traces shown are of multiple runs at the indicated temperatures to show the variability of the data. Average curves were calculated and used for the subsequent kinetics assessment. The inset details the initial region of oxidation and shows that a transition occurs in the first minute of the oxidation reaction in N_2–20% O_2.

rates for each atmosphere; the primary difference being that the inflection, as previously discussed, occurs at a larger specific mass gain with increasing isothermal oxidation temperatures.

As seen by the inflections illustrated in the insets of Figs. 4 and 6 as well as in Fig. 5b, the mechanism for oxidation appears to change after some specific mass gain, which is affected by temperature as well as the oxidation atmosphere. Accordingly, a single oxidation model is not capable of describing the entire oxidation reaction and thus, each of the two regions were defined for individual kinetics assessment in each atmosphere and at each isothermal oxidation temperature. The two regions of differing oxidation behavior in each of the four oxidizing atmospheres are

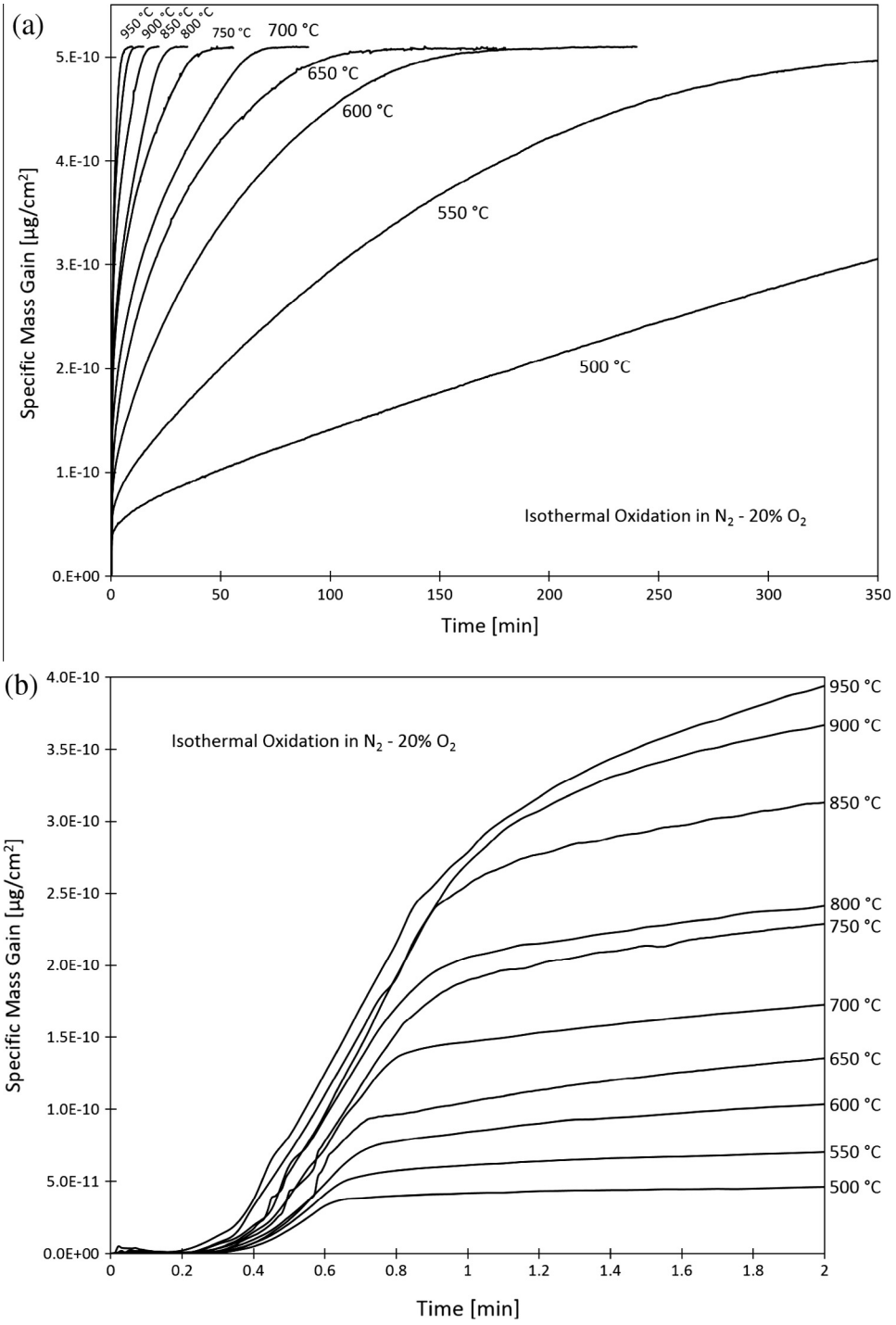

Fig. 5. Isothermal TGA traces describing the oxidation of dysprosium particles in clean air (N_2–20% O_2) from 500 to 950 °C. An inflection is observed in each data set at the beginning of the reaction (b) after an initial region of oxidation where the mechanism is presumed to change into an intermediate region of oxidation. Similar behavior occurs in each of the oxidation atmospheres investigated, as demonstrated in Fig. 6.

quantified in Fig. 7 and labeled as the initial and intermediate regions, respectively. The initial region is defined by the onset of mass gain to the onset of the inflection and the intermediate region begins immediately after the inflection through a reaction extent of 95%, or a specific mass gain of $4.85 \cdot 10^{-10}$ µg/cm^2. Each data point in Fig. 7 corresponds to the average reaction extent, α, defining the end of the initial region of oxidation and the beginning of the intermediate region of oxidation (resulting in a point nearly centered on the inflection in the mass gain data shown in the insets of Figs. 4 and 6 as well as in Fig. 5b). The reaction extent (α) is defined as the ratio of mass gain at time t divided by the total mass gain observed in the oxidation reaction.

An interesting observation from Fig. 7 is that the change in oxidation kinetics (from initial to intermediate reaction kinetics) occurs at lower reaction extents (i.e., the initial oxidation region is a smaller percentage of the overall reaction) in the Ar–20% O_2 oxidizing atmosphere when compared to the nitrogen carrier gases. Additionally, the oxidation reaction is nearly fully defined by the initial reaction region at temperatures equal to and greater than 900, 950, and 1000 °C in N_2–2% O_2, N_2–50% O_2, N_2–20% O_2,

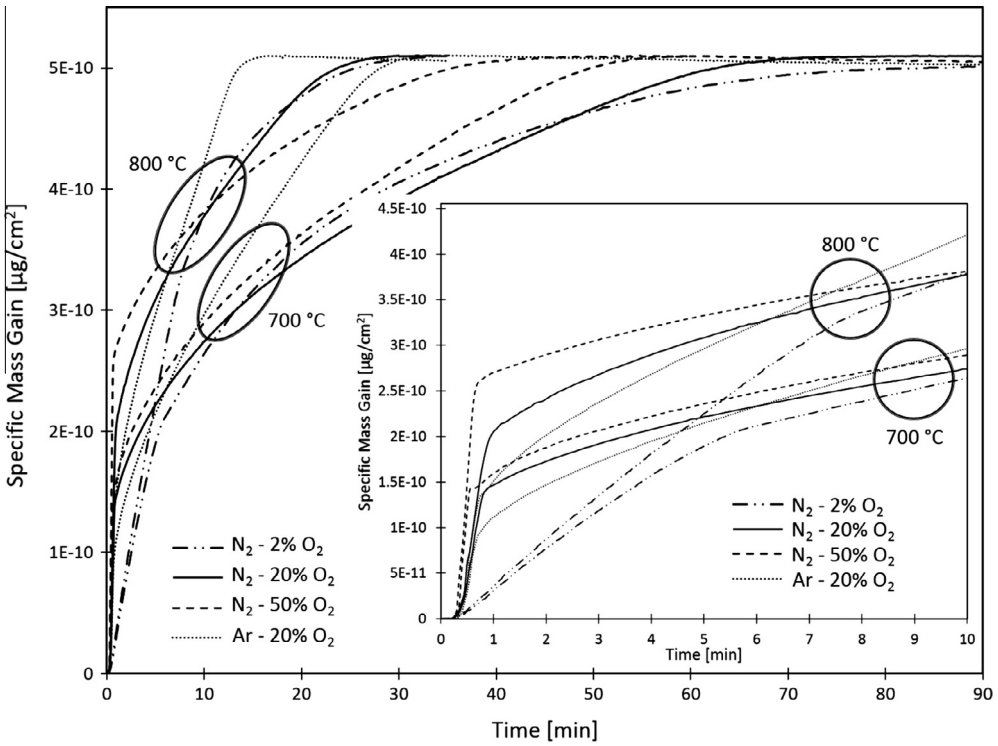

Fig. 6. Isothermal thermogravimetric traces describing the oxidation of dysprosium particles at 700 and 800 °C in each of the atmospheres investigated (N_2–(2%, 20%, or 50%) O_2 and Ar–20% O_2). The inset details the initial region of oxidation and shows that the transition into the intermediate region is delayed in the N_2–2% O_2 atmosphere. The circles are intended to guide the reader to group similar temperature data together.

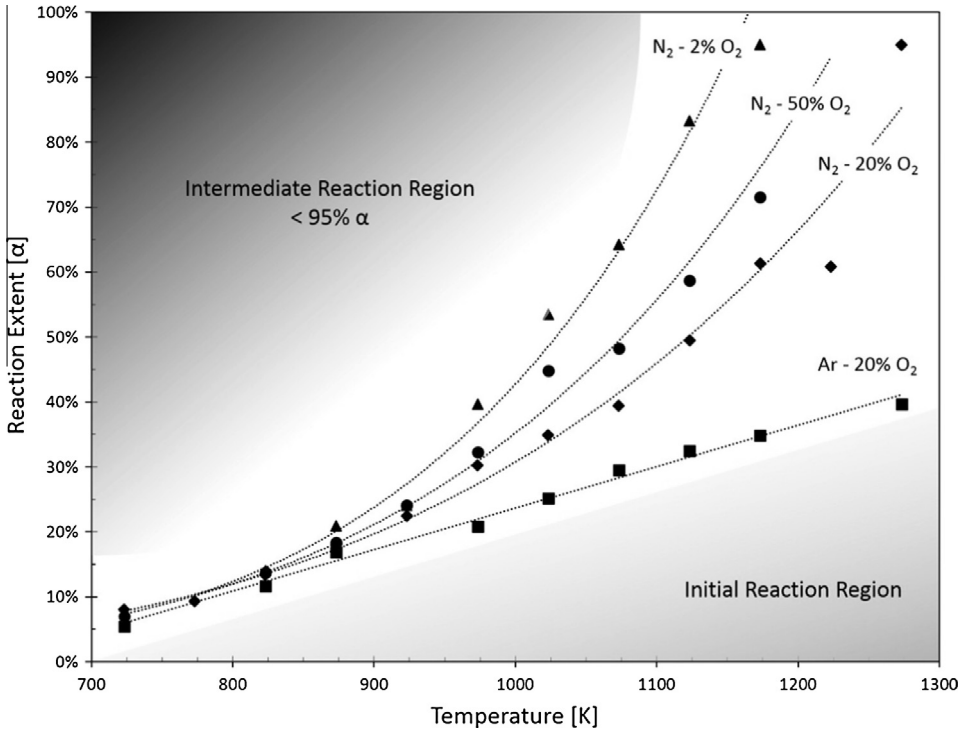

Fig. 7. Plot showing the effect of isothermal oxidation temperature on reaction extent where oxidation kinetics change for each of the oxidation atmospheres investigated (N_2–(2%, 20%, or 50%) O_2 and Ar–20% O_2). Each data point corresponds to the average reaction extent defining the end of the initial oxidation region and the beginning of the intermediate oxidation region (resulting in a point nearly centered on the inflection in the mass gain data shown in the insets of Figs. 4 and 6 as well as in Fig. 5b).

respectively, whereas the initial reaction region comprises only 30–40% of the oxidation reaction at the same temperatures in Ar–20% O_2.

As previously stated, the published literature on the oxidation kinetics of dysprosium is limited; very few publications were found that describe the oxidation kinetics of bulk materials and

none were found describing the behavior of powders or finely distributed particles. Of the literature found, the mechanism of the oxidation reaction is presumed to remain constant over the entire reaction at each temperature, contrary to the results presented here. In a report written by Love [20] in 1959, the rate of dysprosium oxidation was best fit to linear kinetics from 200 to 600 °C in clean air (nearly 20% O_2). However, in the late 1960s Pethe et al. [21] and Greene et al. [22] both reported that the oxidation kinetics follow a parabolic model. Greene et al. presents dysprosium oxidation in temperatures of 300–800 °C in clean air (N_2–20% O_2) and Pethe et al. from 500 to 800 °C in an atmosphere with an oxygen pressure of 100 Torr (13% O_2 at 1 atm total pressure).

In the work presented here, the isothermal oxidation (TGA) data in the initial and intermediate oxidation regions (as defined in Fig. 7) at each temperature and atmosphere were individually fit to many different kinetic models to best determine the kinetics rate constant (k). The models considered included various nucleation models, geometric contraction models, diffusion models, and reaction order models; many of which are described by Khawam et al. [27]. Each of the data sets were fit with each model and the model which best fit the majority of the isothermal oxidation data sets (as determined by a coefficient of determination, or R-squared parameter) was used for the kinetics analysis.

The initial regions of oxidation in each atmosphere was best fit using a contracting area model (also known as a contracting cylinder model), described by:

$$k_{p,i}t = 1 - (1-\alpha)^{\frac{1}{2}} \quad (1)$$

where $k_{p,i}$ is the parabolic rate constant in μg/s cm^2, t is the isothermal oxidation time in seconds, and α is the reaction extent. As previously discussed, the reaction extent (α) was normalized to the maximum value observed after converting to a specific mass gain value with units of μg/cm^2. The contracting area model assumes that nucleation occurs rapidly at the surface of the dysprosium particles and the rate of oxidation is controlled by the resulting reaction interface progressing toward the center of the assumed cylinder [27]. This is a significant assumption considering the morphology of the starting material, as shown in Fig. 1.

As seen in Figs. 5–7, the initial region of the oxidation reaction is confined to a relatively short time period, early in the progression of the overall reaction (less than 1 min in all but the 2% O_2 atmosphere). Since the kinetics in this region are fast, some of the models could only be fit to a few data points, whereas other models (especially in the intermediate region) are defined by many thousands of data points. As seen in Table 1, this fact does not seem to effect the correlation coefficient in the N_2–2% O_2 and N_2–50% O_2 atmospheres, but the correlation coefficient begins to decrease below 700 °C in the N_2–20% O_2 atmosphere and above 700 °C in the Ar–20% O_2 atmosphere. This may suggest a breakdown of the contracting area kinetics model that was empirically chosen, as previously discussed. In the case of the initial region (below 700 °C) of oxidation in the N_2–20% O_2 atmosphere, the model that best fits the TGA data was a nucleation model (the Avrami–Erofeyev (AE2) [27]). However, in the case of the initial region (above 700 °C) of oxidation in the Ar–20% O_2, a better fit was not found.

In a similar manner as described above for the initial region kinetics, the best fit kinetics model in the intermediate region of the oxidation reaction in each of the atmospheres is the Ginstling–Brounshtein diffusion model (a deviation of the Jander model [27]), described by:

$$k_{p,int}t = 1 - \frac{2}{3}\alpha - (1-\alpha)^{\frac{2}{3}} \quad (2)$$

As seen in Table 2, the Ginstling–Brounshtein model correlates well to the oxidation data (TGA) in all atmospheres except for N_2–2% O_2, where geometric contraction models (in particular, a contracting area model) best fit the data.

Similar to the contracting area model used to describe the initial region of oxidation, the Ginstling–Brounshtein model is also a deceleratory model, suggesting that the rate of reaction slows as the reaction extent increases or the available area for reaction decreases. The reaction rate decreases due to the fact that the product layer increases with reaction extent and results in an increasing diffusion distance for cations and/or anions, and thus, slowing the reaction.

In each case, the parabolic rate constant ($k_{p,i}$ and $k_{p,int}$) was determined by plotting the kinetics model (Eqs. (1) and (2)) versus the isothermal reaction time and extracting the slope from a linear relation. As noted previously, the parabolic rate constants for each temperature and atmosphere are listed in Table 1 for the initial oxidation region kinetics and Table 2 for the intermediate oxidation region kinetics.

In order to determine an activation energy for the oxidation reaction in each of the oxidizing atmospheres, the rate constants were plotted using the Arrhenius relation:

$$k_{p,i}, k_{p,int} = Ae^{-\frac{E_a}{RT}} \quad (3)$$

where A is a pre-exponential factor, E_a is the activation energy for the rate limiting mechanism(s) of the oxidation reaction, R is the universal gas constant (8.3145 J/mol K), and T is the absolute temperature in Kelvin. The Arrhenius behavior describing the oxidation of dysprosium particles in the four atmospheres investigated is shown in Fig. 8 for the initial region of oxidation and in Fig. 9 for the intermediate region. As shown in Fig. 9b, unusual oxidation behavior was observed in the N_2–50% O_2 oxidation atmosphere

Table 1
Parabolic rate constants ($k_{p,i}$) and correlation coefficients (R-squared values) for the fits of the oxidation kinetics in the initial oxidation region for all atmospheres using a contracting area model.

Temp (°C)	N_2–2% O_2		N_2–20% O_2		N_2–50% O_2		Ar–20% O_2	
	$k_{p,i}$ * 10^{-7} g^2/cm^4 s	R^2	$k_{p,i}$ * 10^{-7} g^2/cm^4 s	R^2	$k_{p,i}$ * 10^{-7} g^2/cm^4 s	R^2	$k_{p,i}$ * 10^{-7} g^2/cm^4 s	R^2
1000	–		–		–		58.9	0.982
950	–		36.6	0.999	–		–	
900	55.1	0.994	34.0	0.999	71.7	0.991	36.9	0.987
850	3.96	0.997	38.6	0.999	75.1	0.990	35.9	0.980
800	3.77	0.999	32.8	0.996	60.2	0.994	31.0	0.973
750	3.81	0.998	29.8	0.988	53.6	0.998	29.3	0.957
700	3.40	0.997	21.8	0.956	48.0	0.998	24.5	0.988
650	3.60	1.000	16.4	0.986	45.2	1.000	–	
600	2.72	0.998	15.8	0.976	30.2	0.990	17.3	0.992
550	3.15	0.998	12.6	0.970	–		17.9	0.993
500	–		10.5	0.969	–		–	
450	–		6.96	0.979	–		9.27	0.985

Table 2
Parabolic rate constants ($k_{p,int}$) and correlation coefficients (R-squared values) for the fits of the oxidation kinetics in the intermediate oxidation region for all atmospheres using the Ginstling–Brounshtein diffusion model.

Temp (°C)	N_2–2% O_2		N_2–20% O_2		N_2–50% O_2		Ar–20% O_2	
	$k_{p,int} * 10^{-12}$ g^2/cm^4 s	R^2	$k_{p,int} * 10^{-12}$ g^2/cm^4 s	R^2	$k_{p,int} * 10^{-12}$ g^2/cm^4 s	R^2	$k_{p,int} * 10^{-12}$ g^2/cm^4 s	R^2
1000	–		–		–		96.8	0.992
950	–		76.8	0.982	–		–	
900	–		38.8	0.989	22.9	0.970	46.0	1.000
850	31.5	0.978	23.2	0.990	16.3	0.971	41.0	0.995
800	15.5	0.972	17.2	0.997	9.87	0.980	33.2	0.995
750	1.02	0.975	10.7	0.977	8.40	0.988	21.5	0.995
700	6.04	0.959	6.73	0.992	8.37	0.997	16.6	0.999
650	3.42	0.966	4.72	0.976	6.59	0.996	–	
600	1.84	0.984	3.40	0.992	3.87	0.995	5.00	0.995
550	0.93	0.994	1.54	0.992	1.79	0.995	1.39	0.991
500	–		0.528	0.990	–		–	
450	–		0.237	0.996	0.231	0.993	0.290	0.998

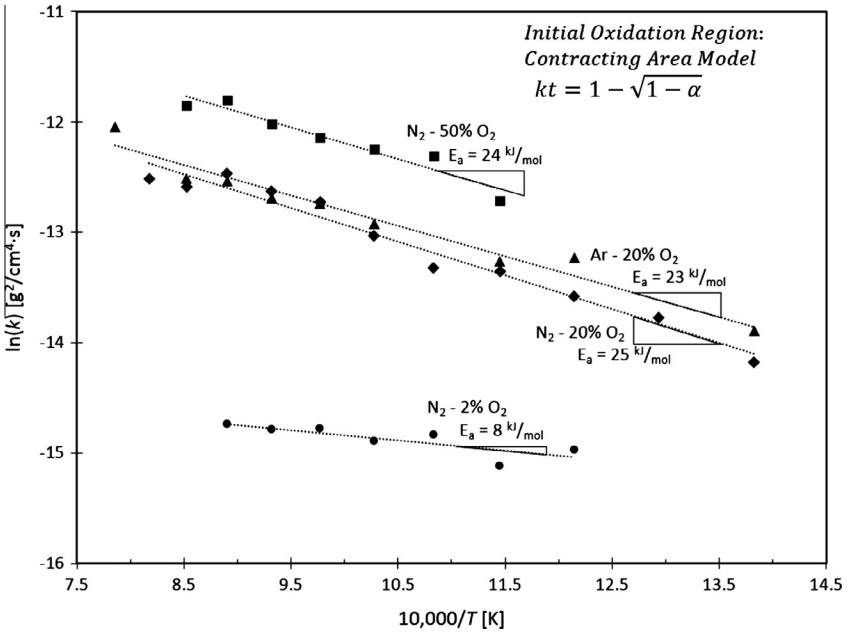

Fig. 8. Arrhenius plot for the initial isothermal oxidation region of dysprosium particles in each of the atmospheres investigated using a contracting area kinetics model. The apparent activation energy is calculated from the linear relation and is labeled for each atmosphere.

where there exists a discontinuity in the reaction kinetics between 650 and 800 °C.

The oxidation rate constants in the initial region of the oxidation reaction were found to be much greater (5–6 orders of magnitude) with a lower apparent activation energy than those found for the intermediate region in each atmosphere. The activation energies in the initial region of oxidation for all of the atmospheres (except the N_2–2% O_2 atmosphere) were found to be approximately 24 kJ/mol (Fig. 8). The value might be compared to the 38 kJ/mol reported by Greene et al. [22], who reported the oxidation of monolithic dysprosium between 300 and 550 °C, but experimental details are lacking which make comparisons difficult. Another interesting trend in Fig. 8 is that samples in the N_2–50% O_2 atmosphere have a rate constant that is nearly twice that of those oxidized in the (Ar, N_2)–20% O_2 atmospheres and more than 10 times that of those oxidized in the N_2–2% O_2 atmosphere. However, the activation energy in the initial reaction region in the 2% oxygen atmosphere was significantly lower, at 8 kJ/mol.

Additionally, the oxidation kinetics in the intermediate region of the oxidation reaction were all found to have an apparent activation energy between 80 and 90 kJ/mol over the temperature range studied, with the exception of the discontinuity observed in the 50% oxygen atmosphere (Fig. 9). The fact that the activation energy in the 2% oxygen atmosphere is slightly higher (90 kJ/mol versus 80 kJ/mol) suggests that the mechanism for oxidation requires slightly more energy (e.g., temperature) than the higher oxygen concentration environments. In any case, these values are fairly similar to those presented by Greene et al. [22] and Pethe et al. [28] who described the overall kinetics of dysprosium oxidation using parabolic kinetics and determined an activation energy of approximately 105 kJ/mol. The discontinuity observed in the 50% oxygen atmosphere, which suggests an apparent activation energy of zero, is indicative of a spontaneous oxidation reaction but is suspected to be anomalous, but repeated, behavior.

In both of the initial and intermediate regions of the isothermal oxidation reaction, it appears that the carrier gas (containing 20% O_2) has minimal effects the oxidation rate of dysprosium based on similar oxidation rate constants (argon results in a rate constant nearly double that observed in nitrogen) and apparent activation energies. However, by comparing the non-isothermal oxidation behavior (Fig. 3) and the selected isothermal behavior (Fig. 6), it is clear that the argon carrier gas promotes more rapid overall oxidation kinetics. This is likely due to the fact that the argon carrier gas induces a transition into the intermediate stage of oxidation at

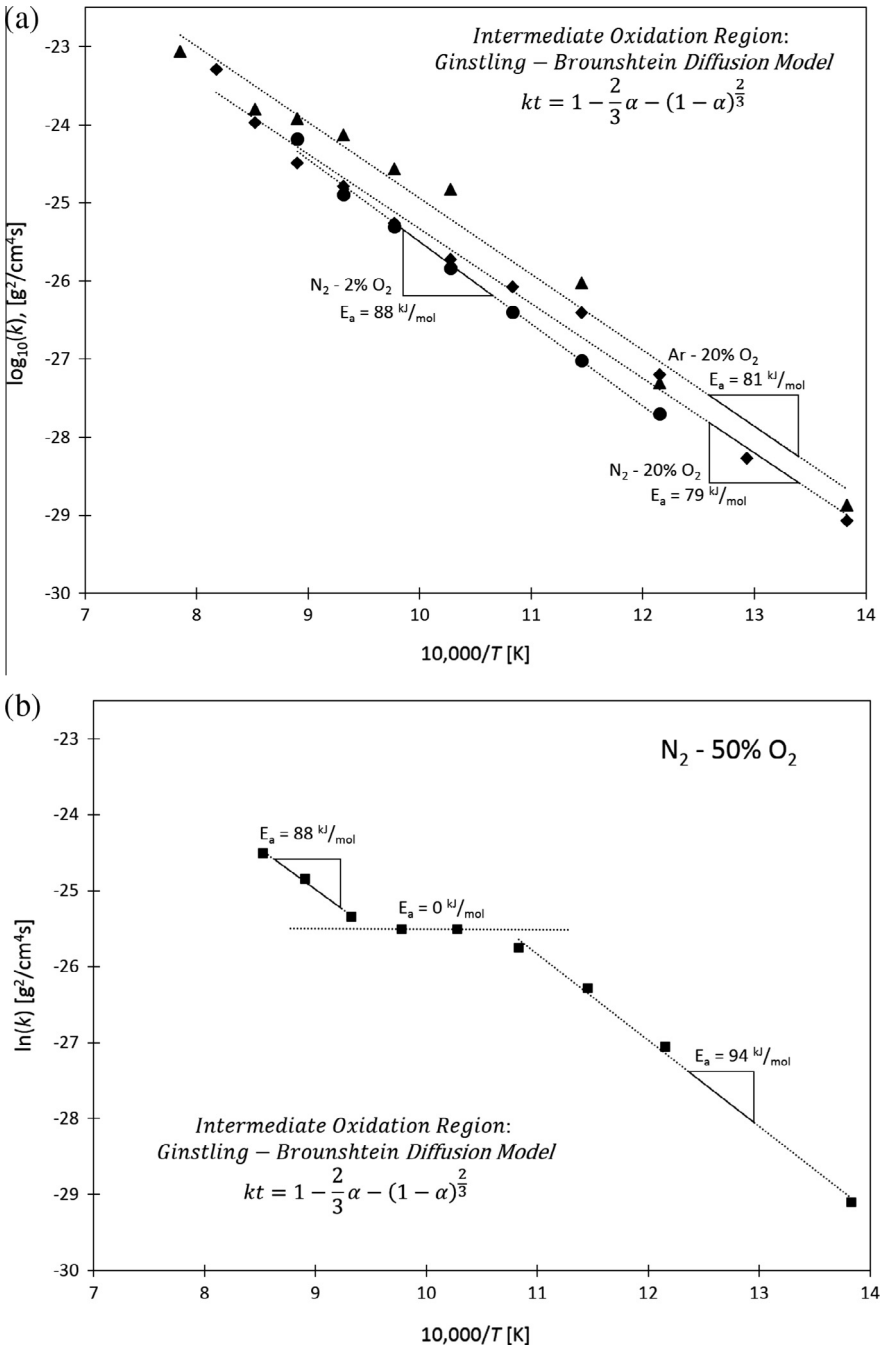

Fig. 9. Arrhenius plots for the intermediate isothermal oxidation region of dysprosium particles in each of the atmospheres investigated using Ginstling–Brounshtein diffusion model. The intermediate region of oxidation of dysprosium in N_2–50% O_2 was isolated from the others due to its interesting behavior, as seen in (b). In each case, the apparent activation energy is calculated from the linear relation and is labeled on each fit.

an earlier reaction extent (Fig. 7) than nitrogen atmospheres. Being that the transition occurs at a lower reaction extent suggests that the initial oxidation layer is thinner, reducing the diffusion length of the oxygen ions, and resulting in faster kinetics in the intermediate region, as observed in Table 2.

A brief, additional study investigating the effects of gas flow rate on the oxidation reaction was performed. In the study, the gas flow rate was increased from 100 to 250 mL/min in an isothermal oxidation temperature range of 650–850 °C. The intermediate region reaction rate and the transition reaction extent (Fig. 7) remained constant, but an effect on the initial region oxidation rate was observed. Although the trends were similar for the initial region oxidation rates, the reaction onset occurred quicker and the rate of oxidation reaction increased with increased gas flow rate. The findings suggest that there is a time delay for the furnace reaction chamber to reach the nominal oxygen concentration of the gas stream. However, the fact that the transition reaction extent remained constant suggests that a critical volume or surface area must be consumed in order for the reaction mechanism to change.

To gain insight into the mechanism of dysprosium oxidation, it is helpful to understand the type of defects present in the oxide. Accordingly, Brouwer diagrams (also referred to as Kroeger–Vink plots [29]) were constructed in each of the identified oxidation

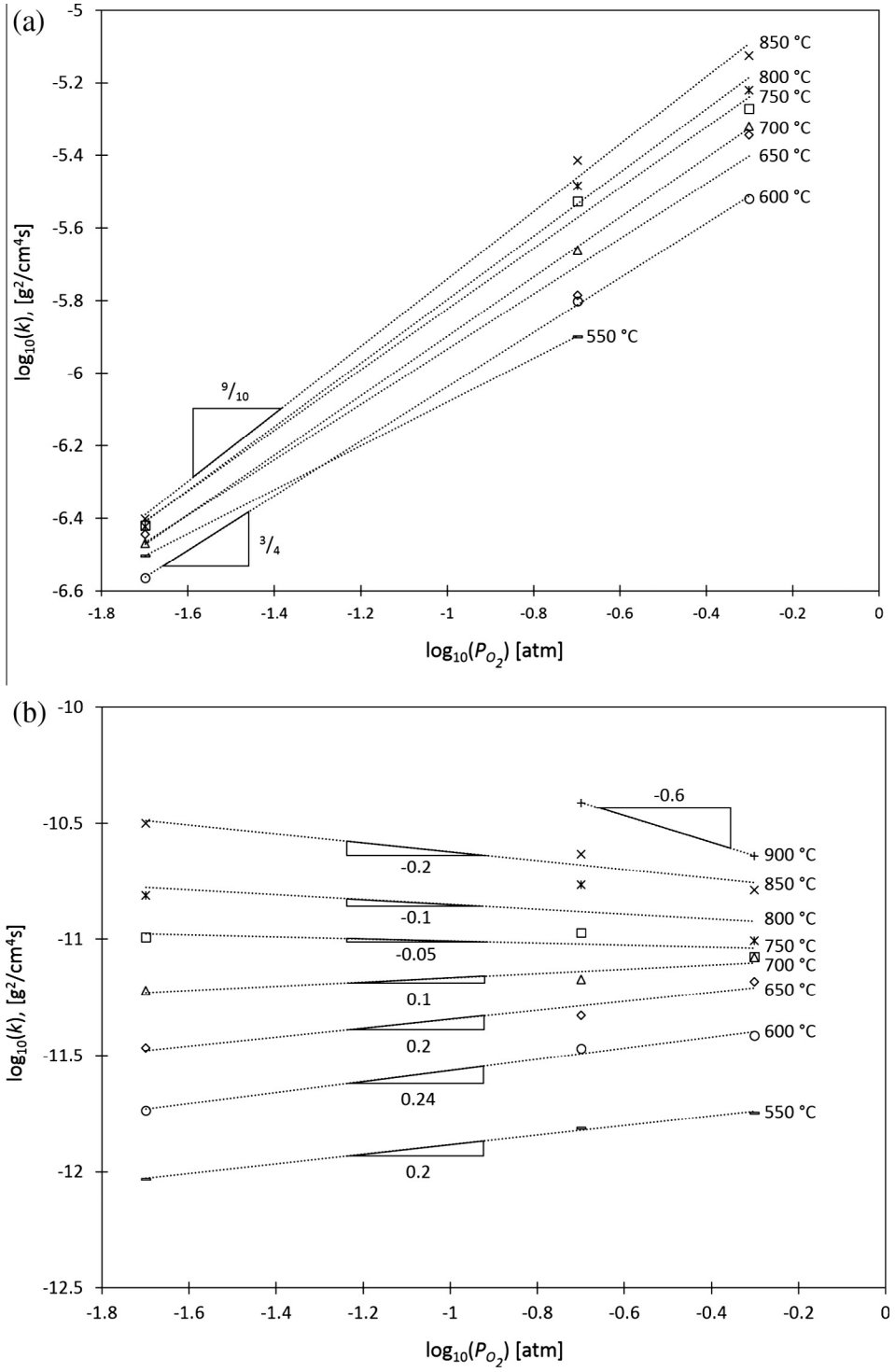

Fig. 10. Kroeger–Vink diagram of the isothermal oxidation of the dysprosium particles showing the dependence of oxygen partial pressure (with a nitrogen carrier gas) on the rate constant in the initial (a) and intermediate (b) regions of oxidation, as described in Fig. 7. The slopes for each linear fit are identified and provide insight into the oxidation mechanism.

regions using the three partial pressures of oxygen used to oxidize dysprosium. As seen in Fig. 10a, the log–log plot in the initial region of oxidation shows a nearly linear dependence of oxygen partial pressure on the rate constant for each temperature studied (600–800 °C). The slope gradually changes from +3/4 to +1 with increasing temperature. Due to the positive slopes over the entire range of temperatures, it is presumed that the oxide behaves as a p-type semiconductor and suggests that the oxidation mechanism is either due to diffusion of oxygen through interstitial sites or dysprosium through vacancies. However, the effects of oxygen pressure on the rate constant in the intermediate region of oxidation is more complicated. As seen in Fig. 10b, which also shows nearly linear correlations, the slope changes from +1/5 to −1/5 from 550 to 850 °C, respectively, with a near zero slope at 750 °C. As was

observed in the initial oxidation region, the positive slope suggests that the oxide acts as a p-type semiconductor in the lower temperature range and as an n-type semiconductor in the high temperature range, with competing defects counteracting each other's charge near 750 °C. An n-type semiconductor suggests that the oxidation mechanism is either due to diffusion of dysprosium through interstitial sites or oxygen through vacancies. Oxygen diffusion is more likely due to the very large size of the dysprosium ions. The n-type behavior was also observed by Tare and Schmalzried [30] from 667 to 860 °C while a later report by Lal et al. [31] suggests that Dy_2O_3 is a p-type semiconductor at 627 °C with a 0.011 $cm^{-2}\,V^{-1}\,s^{-1}$ hole mobility and 0.010 $cm^{-2}\,V^{-1}\,s^{-1}$ electron mobility. Pethe et al. [21] also notes that the parabolic rate constant remains constant (within the experimental error) from 1% to 13% O_2 at 600 °C. However, it is known that minor concentrations of impurities in the starting materials can significantly alter the semiconducting behavior of the oxide. Since impurity concentrations were neither identified nor quantified in previously reported oxidation behavior, comparisons with the work presented here may not be valid. Further work in this area needs to be completed.

To provide further insight into the mechanism of oxidation and to eliminate possible rate limiting defect mechanisms, an inert marker experiment was performed. A thin gold wire was fixed to a nearly 2 mm thick monolithic dysprosium sample which was subsequently oxidized in N_2–20% O_2 at 650 °C for 45 h. The gold marker remained at the oxide/gas interface after oxidation, suggesting that growth occurs at the metal/oxide interface. This observation is consistent with the work of Pethe et al. who found similar behavior via an inert (silver) marker experiment at 800 °C. The results of the marker experiments suggest that when the oxide behaves as a p-type semiconductor, the primary defect mechanism is most likely the diffusion of oxygen via dysprosium vacancies in the oxide and when the oxide behaves as an n-type semiconductor, the primary defect mechanism is likely oxygen diffusion through oxygen vacancies in the oxide.

4. Conclusions

The high temperature oxidation of dysprosium particles in 2–50% oxygen atmospheres in both nitrogen and argon carrier gases was studied from 450 to 1000 °C using both non-isothermal and isothermal techniques. The results of this study have identified two distinct regions of oxidation in each of the four atmospheres investigated, termed the initial and intermediate stages. The reaction rates at 800 °C in the initial oxidation region in N_2–2% O_2, N_2–20% O_2, Ar–20% O_2, N_2–50% O_2, were found using a contracting area model as $10^{-7} * (3.77, 32.8, 31, \text{and } 60.2\ g^2/cm^4\ s)$, respectively. The reaction rates at 800 °C in the intermediate oxidation region in N_2–2% O_2, N_2–20% O_2, Ar–20% O_2, N_2–50% O_2, were found using the Ginstling–Brounshtein diffusion model as $10^{-11} * (15.5, 17.2, 33.2, \text{and } 9.87)\ g^2/cm^4\ s$, respectively. The apparent activation energy was found to be much lower in the initial stages (8 kJ/mol in 2% oxygen and 25 kJ/mol in the 20 and 50% oxygen atmospheres) than in the intermediate stages (80–90 kJ/mol).

Insight into the defect mechanism limiting the kinetics of the oxidation reaction was provided by an inert marker experiment as well as identifying the effects of oxygen pressure on the kinetics rate constant via Kroeger–Vink diagrams. It was determined that oxide growth occurs at the metal/oxide interface, most likely via oxygen diffusion. With the exception of above 750 °C in the intermediate oxidation region, the oxide behaves as a p-type semiconductor. The conclusion drawn from the evidence provided is that the rate limiting oxidation mechanism is oxygen diffusion via dysprosium vacancies to grow at the Dy/Dy_2O_3 interface. In the cases where the oxide behaves as an n-type semiconductor, oxidation is primarily rate limited by oxygen ion diffusion via oxygen vacancies to the Dy/Dy_2O_3 interface. However, further studies are needed to better understand the effects of impurity types and concentrations on the semiconducting properties of the oxide layer.

Acknowledgements

The authors would also like to acknowledge Nicole Leraas and Kelci Lester for their contributions and helpful discussions.

References

[1] J.S. Thomason, R.J. Atwell, Y. Bajraktari, J.P. Bell, D.S. Barnett, N.S.J. Karvonides, M.F. Niles, E.L. Schwartz, From National Defense Stockpile (NDS) to Strategic Materials Security Program (SMSP): Evidence and Analytic Support, Institute for Defense Analysis, 2010.
[2] S. Hoenderdaal, L.T. Espinoza, F. Marscheider-Weidemann, W. Graus, Can a dysprosium shortage threaten green energy technologies?, Energy 49 (2013) 344–355
[3] W.M. Haynes (Ed.), CRC Handbook of Chemistry and Physics, CRC Press/Taylor and Francis, Boca Raton, FL, 2014.
[4] B.T. Kilbourn, A Lanthanide Lanthology: Part I, A-L, Molycorp, Inc., Fairfield, NJ, USA, 1993.
[5] H. Il Kim, M. Herman, S.F. Mughabghab, P. Oblozinsky, Y.O. Lee, Evaluation of neutron cross sections for a complete set of Dy isotopes, Nucl. Instrum. Methods Phys. Res. Sect. B-Beam Interact. Mater. Atoms 266 (2008) 3513–3528.
[6] N. Dzysiuk, A. Kadenko, I. Kadenko, G. Primenko, Measurement and systematic study of (n, x) cross sections for dysprosium (Dy), erbium (Er), and ytterbium (Yb) isotopes at 14.7 MeV neutron energy, Phys. Rev. C 86 (2012) 10.
[7] O.S. Youl, G.C. Sup, J. Chang, Evaluation of neutron cross sections of Dy isotopes in the resonance region, J. Korean Nucl. Soc. 33 (2001) 46–61.
[8] H. Saghrouni, S. Jomni, W. Belgacem, N. Hamdaoui, L. Beji, Physical and electrical characteristics of metal/Dy_2O_3/p-GaAs structure, Phys. B-Condens. Matter 444 (2014) 58–64.
[9] A. Cherif, S. Jomni, W. Belgacem, R. Hannachi, N. Mliki, L. Beji, Investigation of structural properties, electrical and dielectrical characteristics of A1/Dy_2O_3/porous Si heterostructure, Superlattices Microstruct. 68 (2014) 76–89.
[10] D.P. Butt, B.J. Jaques, D.D. Osterberg, B.M. Marx, P.G. Callahan, A.S. Hamdy, New routes to lanthanide and actinide nitrides, in: GLOBAL 2009: The Nuclear Fuel Cycle: Sustainable Options and Industrial Perspectives, September 6, 2009–September 11, 2009, Paris, France, 2009.
[11] B.J. Jaques, D.P. Butt, B.M. Marx, A.S. Hamdy, D. Osterberg, G. Balfour, Synthesis and characterization of actinide nitrides, in: GLOBAL 2007: Advanced Nuclear Fuel Cycles and Systems, September 9, 2007–September 13, 2007, American Nuclear Society, Boise, ID, United States, 2007, pp. 591–596.
[12] B.J. Jaques, B.M. Marx, A.S. Hamdy, D.P. Butt, Synthesis of uranium nitride by a mechanically induced gas–solid reaction, J. Nucl. Mater. 381 (2008) 309–311.
[13] P.G. Callahan, B.J. Jaques, B.M. Marx, A.S. Hamdy, D.P. Butt, Synthesis of dysprosium and cerium nitrides by a mechanically induced gas–solid reaction, J. Nucl. Mater. 392 (2009) 121–124.
[14] M. Takano, A. Itoh, M. Akabori, K. Minato, Hydrolysis reactions of rare-earth and americium mononitrides, J. Phys. Chem. Solids 66 (2005) 697–700.
[15] M. Takano, S. Tagami, K. Minato, T. Kozaki, S. Sato, Lattice thermal expansions of (Dy, Zr)N solid solutions, J. Alloys Comp. 439 (2007) 215–220.
[16] Y.K. Zhou, M.S. Kim, N. Teraguchi, A. Suzuki, Y. Nanishi, H. Asahi, Optical and magnetic properties of the DyN/GaN superlattice, Phys. Status Solidi B-Basic Res. 240 (2003) 440–442.
[17] T.B. Thiede, M. Krasnopolski, A.P. Milanov, T. de los Arcos, A. Ney, H.W. Becker, D. Rogalla, J. Winter, A. Devi, R.A. Fischeri, Evaluation of homoleptic guanidinate and amidinate complexes of gadolinium and dysprosium for MOCVD of rare-earth nitride thin films, Chem. Mater. 23 (2011) 1430–1440.
[18] X.J. Li, Y.K. Zhou, M. Kim, S. Kimura, N. Teraguchi, S. Emura, S. Hasegawa, H. Asahi, Magnetic and transport properties of ferromagnetic semiconductor GaDyN thin film, Chin. Phys. Lett. 22 (2005) 463–465.
[19] B. Love, Selection and Evaluation of Rare or Unusual Metals for Application to Advanced Weapons Systems. Part I: A Literature Survey, Wright Air Development Center, 1958.
[20] B. Love, Selection and Evaluation of Rare or Unusual Metals for Application to Advanced Weapons Systems. Part II: The Metallurgy of Yttrium and the Rare Earth Metals, Wright Air Development Center, 1959.
[21] L.D. Pethe, H.B. Mathur, A.B. Biswas, Kinetics of oxidation of dysprosium metal in the temperature region 500–800 °C, Indian J. Chem. 6 (1968) 156–158.
[22] N.D. Greene, F.G. Hodge, Oxidation characteristics of the lanthanide metals, Corrosion 22 (1966) 206–216.
[23] F.H. Spedding, J.J. Hanak, A.H. Daane, High temperature allotropy and thermal expansion of the rare-earth metals, J. Less-Common Met. 3 (1961) 110–124.
[24] A.E. Curzon, H.G. Chlebek, The observation of face centred cubic Gd, Tb, Dy, Ho, Er and Tm in the form of thin films and their oxidation, J. Phys. F (Met. Phys.) 3 (1973) 1–5.
[25] H.E. Swanson, M.I. Cook, T. Isaacs, E.H. Evans, Standard X-ray diffraction powder patterns, U.S. Dept. of Commerce, National Bureau of Standards Circular 539, Washington, DC, 1959.

[26] T.H. Okabe, K. Hirota, E. Kasai, F. Saito, Y. Waseda, K.T. Jacob, Thermodynamic properties of oxygen in RE-O (RE = Gd, Tb, Dy, Er) solid solutions, J. Alloys Comp. 279 (1998) 184–191.
[27] A. Khawam, D.R. Flanagan, Solid-state kinetic models: basics and mathematical fundamentals, J. Phys. Chem. B 110 (2006) 17315–17328.
[28] L.D. Pethe, H.B. Mathur, A.B. Biswas, High temperature oxidation kinetics of lanthanum metal, Indian J. Chem. 5 (1967) 427–429.
[29] A.S. Khanna, Introduction to High Temperature Oxidation and Corrosion, ASM International, Materials Park, OH, 2002.
[30] V.B. Tare, H. Schmalzried, Ionic and electronic conductivity in some rare earth oxides, Z. Phys. Chem., Neue Fol. 43 (1964) 30–32.
[31] H.B. Lal, K. Gaur, Electrical conduction in non-metallic rare-earth solids, J. Mater. Sci. 23 (1988) 919–923.